PCCP

ROYAL SOCIETY OF CHEMISTRY

PAPER

View Article Online
View Journal | View Issue

Cite this: *Phys. Chem. Chem. Phys.*, 2020, **22**, 10238

Pressure-induced structural transformations and new polymorphs in $BiVO_4$† HPSTAR 960-2020

Xuerui Cheng,[a] Jiwen Guan,[b] Liying Jiang,[c] Huanjun Zhang,[a] Pan Wang,[d] Adebayo O. Adeniyi,[e] Yansun Yao,[e] Lei Su*[f] and Yang Song*[bd]

Received 6th March 2020,
Accepted 15th April 2020

DOI: 10.1039/d0cp01274b

rsc.li/pccp

$BiVO_4$ has attracted much attention in recent years due to its active photocatalytic and microwave dielectric properties. $BiVO_4$ exhibits a rich structural polymorphism, and its properties strongly depend on the crystalline phase. Therefore, it is of great importance to achieve an easy control of its crystalline phase. In the present work, phase stability and vibrational properties of fergusonite- and zircon-type $BiVO_4$ are investigated up to 41.6 GPa by *in situ* synchrotron X-ray diffraction (XRD), Raman spectroscopy, and first principles calculation. Upon compression, although having different initial structures, both types of $BiVO_4$ consecutively transform to scheelite- and β-fergusonite structures. For the first time reported for $BiVO_4$, the β-fergusonite structure is determined using first principles computational techniques and from refinement of the XRD data. Along the way, one new phase of $BiVO_4$ is theoretically predicted at higher pressures. Moreover, both the fergusonite-to-scheelite and scheelite-to-β-fergusonite transitions are reversible, while the zircon-to-scheelite transition is irreversible. A large volume collapse is observed associated with each phase transition, and the equations of state for different types of $BiVO_4$ have been determined. These results provide new insights into the relationship between different structural types in the AVO_4 family.

1. Introduction

Recently, as an ideal semiconductor photocatalyst, bismuth vanadate ($BiVO_4$) has drawn great attention because of its promising photocatalytic properties.[1–3] $BiVO_4$ exhibits a rich structural polymorphism, and three main crystalline phases have been observed, namely, the tetragonal zircon structure (tz-$BiVO_4$, $I4_1/amd$), monoclinic fergusonite structure (mf-$BiVO_4$, $I2/a$) and the tetragonal scheelite structure (ts-$BiVO_4$, $I4_1/a$).[4,5] Among these structures, mf-$BiVO_4$ shows excellent photocatalytic activity, while tz-$BiVO_4$ and ts-$BiVO_4$ exhibit relatively poor photocatalytic activity.[6,7] Thus, mf-$BiVO_4$ is not considered as an excellent phosphor host compared to tz-$BiVO_4$.[8] Therefore, the properties of $BiVO_4$ depend strongly on the crystalline structure. For practical applications, it is of great importance to achieve an easy control of the crystal phase of $BiVO_4$.

Generally, tz-$BiVO_4$ can be prepared in aqueous media by a low-temperature process. Tz-$BiVO_4$ can transform to mf-$BiVO_4$ after heat treatment at 600–770 K by an irreversible transition.[9] Besides temperature, pressure has also been extensively used to discover and access new structures and/or novel properties of materials.[10,11] The structural stability and phase transition of orthovanadate compounds have been explored under high pressure. Most orthovanadates exist in zircon or scheelite structures under ambient conditions.[12–19] For most zircon-type orthovanadate compounds, such as $HoVO_4$, $TbVO_4$ and $LuVO_4$, a pressure-induced irreversible transition to a scheelite structure is known, while several zircon structures with a larger cation, such as $NdVO_4$ and $PrVO_4$, undergo a zircon-to-monazite transition.[14–16,19] In contrast, scheelite-type orthovanadates, such as $GdVO_4$ and $ScVO_4$, have been observed to transform into the fergusonite structure.[12,13]

Different from most orthovanadates, $BiVO_4$ adopts a fergusonite structure rather than a zircon or scheelite structure under ambient conditions. Therefore, it may exhibit different behaviors under pressure. It has been previously reported that mf-$BiVO_4$ would transform to ts-$BiVO_4$ above 1.7 GPa.[20–22] However, its pressure range is too low. Recently, it was reported that both mf-$BiVO_4$ and tz-$BiVO_4$ can transform to ts-$BiVO_4$ and

[a] *School of Physics and Electronic Engineering, Zhengzhou University of Light Industry, Zhengzhou, Henan, 450002, P. R. China*
[b] *Department of Physics and Astronomy, University of Western Ontario, London, Ontario N6A 3K7, Canada*
[c] *College of Electrical and Information Engineering, Zhengzhou University of Light Industry, Zhengzhou, Henan 450002, P. R. China*
[d] *Department of Chemistry, University of Western Ontario, London, Ontario N6A 5B7, Canada. E-mail: yang.song@uwo.ca*
[e] *Department of Physics and Engineering Physics, University of Saskatchewan, Saskatoon, Saskatchewan S7N 5E2, Canada*
[f] *Center for High Pressure Science and Technology Advanced Research, 100094 Beijing, P. R. China. E-mail: leisu2050@iccas.ac.cn*

† Electronic supplementary information (ESI) available. See DOI: 10.1039/d0cp01274b

then a new structural change was observed above 15.7 GPa.[11] But this new structure cannot be confirmed because of the lack of high-pressure (HP) X-ray diffraction (XRD) data. In another recent study, phase transitions of fergusonite–scheelite-$P2_1/n$ were reported from *in situ* synchrotron XRD analysis for fergusonite-type $Eu_{0.1}Bi_{0.9}VO_4$.[23] Therefore, the $P2_1/n$ structure may be speculated to be the second high pressure phase for mf-$BiVO_4$. However, it is well known that doping can induce lattice distortions and reduce the stability of the structure, resulting in a significant effect on the phase transition. With increasing pressure, for example, Y_2O_3 showed a cubic–hexagonal transition, while Y_2O_3:Eu exhibited a cubic–monoclinic–hexagonal structure sequence.[24] Different phase transition sequences have also been observed between other pure and doped samples, such as $BiFeO_3$ and $BiFeO_3$:Ba, SnO_2 and SnO_2:Fe.[25–27] Particularly for mf-$BiVO_4$, it has been reported that lanthanide doping can trigger phase transformation from mf-$BiVO_4$ to tetragonal tz-$BiVO_4$.[7,28–30] More interestingly, after decompression, one mixed phase has been reported for mf-$BiVO_4$, which has not been observed in mf-$Eu_{0.1}Bi_{0.9}VO_4$.[11,23] Whether this is associated with a phase transition or decomposition could not be confirmed. Furthermore, the high-pressure behavior of zircon-type $BiVO_4$ needs further confirmation, especially using *in situ* synchrotron XRD. Thus, there are uncharted structural changes for $BiVO_4$, so it is necessary to extend the previous studies to fully understand the structural stability and polymorphs of $BiVO_4$ under high pressure, especially to precisely determine the crystal structures using high-pressure XRD.

In view of this aim, in this work, fergusonite- and zircon-type $BiVO_4$ are successfully synthetized using the hydrothermal method. Then, *in situ* high-pressure XRD and Raman experiments are performed at room temperature. Several phase transitions are observed including the one to a new crystalline phase. The structure of the new phase was characterized using *ab initio* computational techniques. These results reveal a microscopic picture of the pressure-induced phase transition nature for the fergusonite- and zircon-type ABO_4 compounds and provide insights into underlying structure–property relationships of $BiVO_4$.

2. Experimental and theoretical methods

2.1 Sample preparation

Pure mf- and tz-$BiVO_4$ samples were synthesized using the hydrothermal method.[30,31] The starting materials were $Bi(NO_3)_3{\cdot}5H_2O$ and NH_4VO_3 with a purity of 99.9%. First, 2.43 g of $Bi(NO_3)_3{\cdot}5H_2O$ was dissolved into 25 mL of 2.0 mol L^{-1} HNO_3, which was marked as solution-A, while 0.58 g of NH_4VO_3 was dissolved into 10.0 mL of 5.0 mol L^{-1} NaOH, which was marked as solution-B. Then, solution-B was added dropwise to solution-A under constant magnetic stirring. After stirring for 30 min, some amount of 1 mol L^{-1} NaOH aqueous solution was added dropwise with stirring to tune the final pH of the growth solution to 5.0. Then, the suspension was stirred for another 10 min and poured into a 50 mL Teflon-lined stainless autoclave. Subsequently, it was sealed at 220 °C for 10 hours, and then allowed to cool to room temperature naturally. Finally, the precipitation was separated by centrifugation, washed with distilled water and absolute ethanol, and dried at 80 °C to obtain the tz-$BiVO_4$ sample. Part of the tz-$BiVO_4$ sample was annealed at 600 °C for 10 hours to transform into the mf-$BiVO_4$ sample. The crystal structures of the two samples were firstly identified by X-ray diffraction using Cu Kα radiation (1.5418 Å). The XRD and Raman results confirmed the successful synthesis of mf- and tz-$BiVO_4$ samples, as shown in Fig. S1 and S2 (ESI†).

2.2 High-pressure measurements

The high-pressure experiment was carried out to the sample in a diamond anvil cell (DAC), with two diamonds of 350 micron size. The pressure was measured by the shift of the R1 photoluminescence line of ruby.[32,33] The Raman measurements were performed by using a Renishaw InVia Raman microscope with a 532 nm laser. The power of the laser is 5 mW to avoid the laser heating effect. *In situ* XRD experiments were performed at the 16-BMD beamline of the HPCAT facility at the Advanced Photon Source (APS) using monochromatic radiation with λ = 0.4959 Å. Diffraction images were recorded using a Mar345 image plate detector, 230 mm away from the sample, and were integrated and corrected for distortions using the FIT2D software. Argon (Ar) was used as the pressure transmitting medium (PTM) for high-pressure Raman spectroscopy, while silicon oil was used as the PTM for XRD.

2.3 Computational methods

Pressure-induced phase transitions of $BiVO_4$ were simulated using the metadynamics method[34,35] combined with the projector augmented plane-wave (PAW) method[36] as implemented in the Vienna Ab Initio Simulation (VASP) program.[37] PAW potentials with the Perdew–Burke–Ernzerhof (PBE) functional[38] and a 500 eV energy cutoff were used. The Bi, V, and O potentials employ $5d^{10}6s^26p^3$, $3s^23p^63d^34s^2$, and $2s^22p^4$ as valence states, respectively. Each metastep consisted of a first principles molecular dynamics (MD) simulation within the canonical (*NVT*) ensemble for a simulation time of 0.4 ps, along with a *k*-spacing of $2\pi \times 0.08$ Å^{-1} for the Brillouin zone (BZ) sampling. To reduce the energy barrier for phase transitions, the supercells were over-pressurized under both hydrostatic and non-hydrostatic conditions. A recent implementation[39] was used to load the uniaxial stresses to the simulation cell. Enthalpy calculation for candidate structures was conducted with a fine *k*-spacing of $2\pi \times 0.03$ Å^{-1}, which yielded excellent convergence for total energy (within 1 meV per atom). Phonon dispersion relations were calculated using the density functional perturbation theory[40] and post processed using the PHONOPY code.[41]

3 Results and discussion

3.1 High-pressure Raman spectra of $BiVO_4$

The Raman spectra of the prepared $BiVO_4$ samples measured under ambient conditions are presented in Fig. S2 (ESI†).

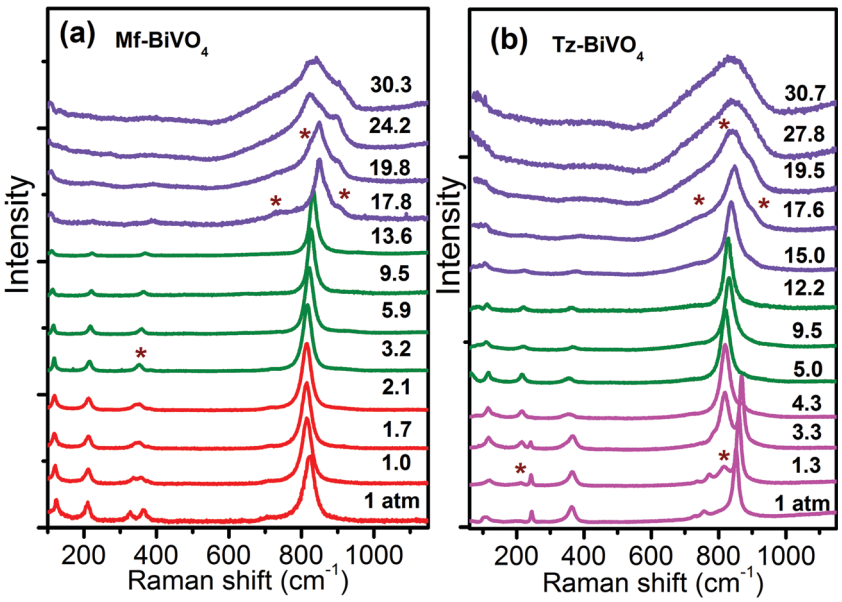

Fig. 1 Selected high-pressure Raman spectra of (a) mf-$BiVO_4$ and (b) tz-$BiVO_4$ upon compression. The pressures in GPa are labelled for each spectrum. The asterisks denote the new modes that emerged.

The assignments of Raman active modes confirm that the prepared samples are indeed in fergusonite- and zircon-type structures.[2,9,42] For mf-$BiVO_4$, upon compression, a fergusonite-to-scheelite transition is observed above 2.1 GPa, as shown in Fig. 1(a).[20–22] Fergusonite is a weakly distorted version of the scheelite structure, and therefore most Raman modes are retained during this transition.[11] After phase transition, two otherwise split lines (323.5 and 365.6 cm^{-1}) in mf-$BiVO_4$ gradually merge into one peak. Upon subsequent compression to 13.6 GPa, no other change is detected, except for a phonon softening observed at 116.3 cm^{-1}. Above 17.8 GPa, three new modes emerge at 734.6, 860, and 905.8 cm^{-1}, and their intensity gradually increased during the compression, as marked in Fig. 1(a). Simultaneously, the original modes of ts-$BiVO_4$ become weaker and several modes finally become unresolvable at higher pressure. Moreover, pressure-induced broadening is observed above 13.6 GPa because of the non-hydrostatic condition at high pressure. A similar phase transition was also observed for tz-$BiVO_4$, as shown in Fig. 1(b). A new phase emerges at 1.3 GPa and coexists with the zircon phase until 5.0 GPa. By comparing the Raman spectra of the pure new phase above 5.0 GPa to those of known structures, we found that the new phase is also ts-$BiVO_4$. Similar to mf-$BiVO_4$, upon further increasing the pressure above 15.0 GPa, three new bands appeared, and the intensity of the original peaks became somewhat weak with increasing pressure, implying that another structural change has occurred.

The structural evolution of mf-$BiVO_4$ and tz-$BiVO_4$ was further established from the pressure dependence of the mode frequencies. As shown in Fig. 2(a) and (b), two inflection points are clearly observed at 3.2 and 17.8 GPa for mf-$BiVO_4$, while four pressure regions with different structural characters are observed for tz-$BiVO_4$. Although the mf- and tz-$BiVO_4$ phases have different structures, both exhibit similar structural evolution and transform into ts-$BiVO_4$ at high pressure. However, the range of stability for ts-$BiVO_4$ is small. Above 15 GPa, the second structure transition occurs in both samples, as confirmed by the appearance of several new modes in the Raman spectra, which agrees well with a previous report.[11] However, the previous report could not conclude whether this change corresponds to a phase transition or decomposition.[11] Thus, it is necessary to investigate the structural evolution upon decompression, because such structural changes would not be reversible if decomposition has happened.

The Raman spectra of both samples upon decompression are shown in Fig. 3. For comparison, the Raman spectra of the original mf-$BiVO_4$ and tz-$BiVO_4$ are also presented. The results show that the two samples exhibit the same structural evolution during decompression. Both high-pressure structures (yet to be determined) obtained by compressing mf-$BiVO_4$ and tz-$BiVO_4$ transform back to the same ts-$BiVO_4$ phase when the pressure is released, at 13.8 and 12.1 GPa, respectively. Upon decompressing further, both samples finally transform back to mf-$BiVO_4$ below 2 GPa, which can be clearly distinguished from the characteristic splitting modes at 323.5 cm^{-1} and 365.6 cm^{-1}. The initial structure of tz-$BiVO_4$ was not observed after pressure release. This result is quite different from the previous report that a mixed phase was obtained after pressure release.[11] From the current observation, a reversible phase transition for mf-$BiVO_4$ during decompression provides a direct explanation for phase transition rather than decomposition. Going further, we need to determine the structures for both high-pressure phases, in particular the newly discovered phase, using synchrotron XRD measurement.

3.2 High-pressure XRD of $BiVO_4$

The evolutions of the XRD pattern during the compression of two types of $BiVO_4$ followed by a decompression to ambient

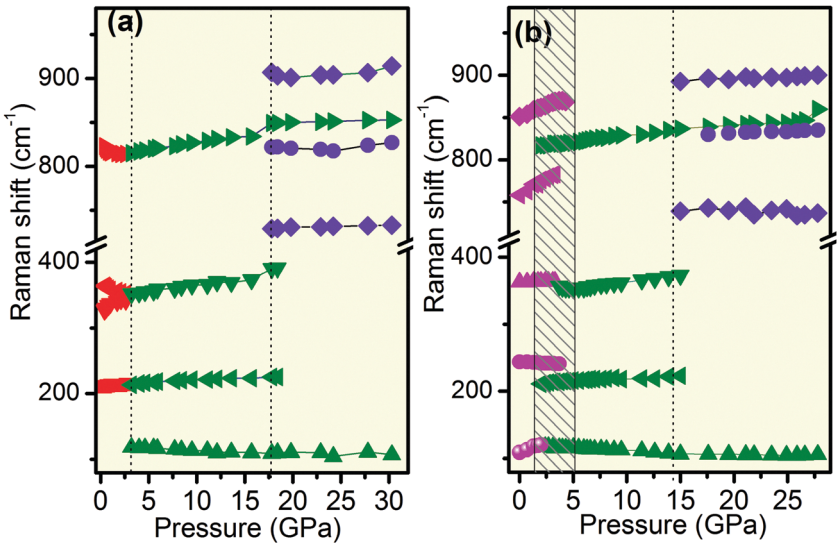

Fig. 2 Pressure dependence of the Raman mode frequencies of (a) mf-$BiVO_4$ and (b) tz-$BiVO_4$ upon compression.

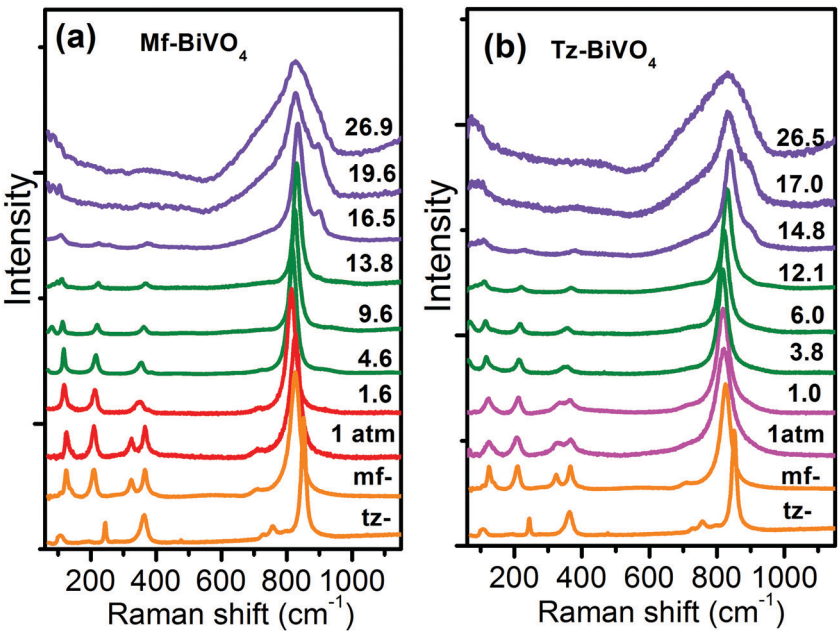

Fig. 3 Selected Raman spectra of (a) mf-$BiVO_4$ and (b) tz-$BiVO_4$ upon decompression. For comparison, the Raman spectra of mf-$BiVO_4$ and tz-$BiVO_4$ are also shown as a reference.

pressure are shown in Fig. 4. A Rietveld refinement of the XRD patterns was performed using the GSAS software package, as illustrated in Fig. 4(c), while the detailed refinement results are listed in Table 1. For the tz-$BiVO_4$ sample, the original diffraction peaks disappear, and several new peaks appear at 6.4 GPa, indicating the first phase transition. From the Rietveld refinement, this HP phase is identified as the scheelite structure (ts-$BiVO_4$), in agreement with the Raman results. The different transition pressures obtained from the Raman results may stem from the effect of the different PTMs. Although the PTM effect is not desirable, it does not influence refinement results significantly. Upon further increasing the pressure to 17.4 GPa, several new diffraction peaks appear at 5.9°, 6.4° and 9.9° (2θ), signaling the second phase transition. Upon further compression, the new peaks gradually grow in intensity, while simultaneously the peaks of ts-$BiVO_4$ gradually decrease, forming a region of two-phase coexistence.

To identify the post-scheelite structure, first-principles metadynamics simulations were performed. The simulations were carried out at room temperature and at four pressures, *e.g.*, 25, 30, 35, and 40 GPa, starting from a $2 \times 2 \times 2$ ts-$BiVO_4$ supercell. In the simulations, the structure was overcompressed to allow for a faster reaction. A little to our surprise, the first phase transition was obtained at 30 GPa, where ts-$BiVO_4$

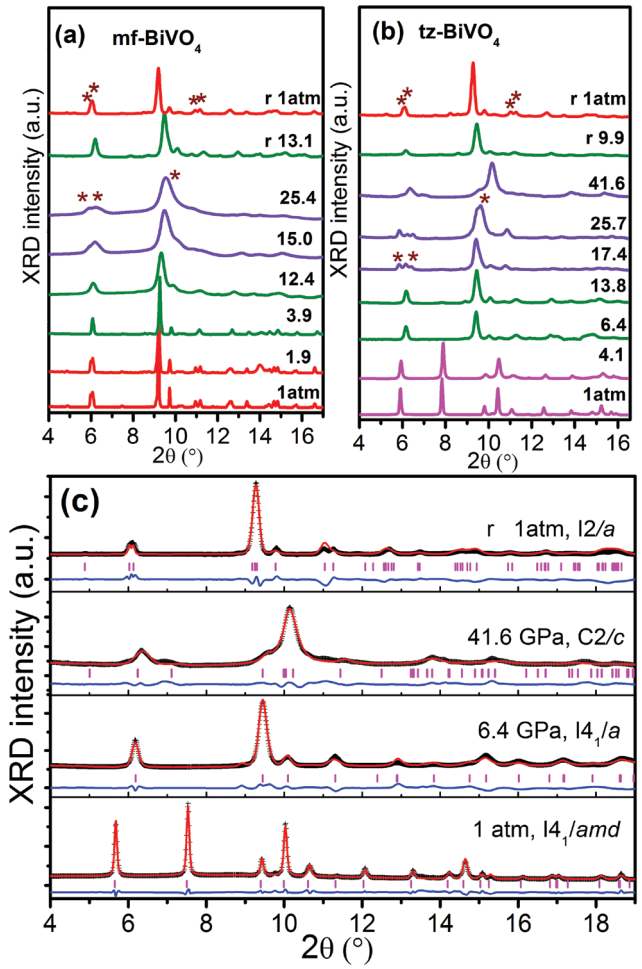

Fig. 4 XRD patterns of (a) mf-$BiVO_4$ and (b) tz-$BiVO_4$ at several selected pressures (in GPa) upon compression to 25.4 and 41.6 GPa, respectively, followed by decompression to ambient pressure (1 atm). (c) Rietveld refinement of the diffraction patterns of tz-$BiVO_4$. The experimental data are shown as black crosses with refinements shown as red solid lines and the difference between calculated and observed intensities is shown as blue lines. Ticks indicate the positions of Bragg peaks.

transforms directly to a new structure with the $C2/c$ space group, rather than the $P2_1/n$ structure reported for $Eu_{0.1}Bi_{0.9}VO_4$.[23] Comparing with the known structures in the literature shows that this $C2/c$ structure is isostructural to β-fergusonite, which has also been observed at high pressure in wolframite $ZnWO_4$.[44] To confirm the structure of the post-scheelite phase, we used both $P2_1/n$ and $C2/c$ (β-fergusonite) structural models to refine the XRD patterns. As can be seen in Fig. S3 (ESI†), the β-fergusonite mode fits the diffraction pattern very well. Moreover, the values of R_p and R_{wp} further suggest that the β-fergusonite mode is more suitable. In addition, the XRD pattern collected at 41.6 GPa can be well refined to a single β-fergusonite structure, as shown in Fig. 4(c), and the unit cell parameters obtained are listed in Table 1.

A similar result was also observed in mf-$BiVO_4$ up to the maximum pressure of 25.4 GPa. But its spectra are broader at high pressure, which may stem from the non-hydrostatic conditions. Both kinds of $BiVO_4$ share the same structural evolution under high pressure. When the pressure is released in β-fergusonite, the scheelite phase appears again, at pressures below 13.1 GPa. Drastic splitting is observed in several diffraction peaks below 2 GPa, such as 6.1° and 11.1° 2θ, as marked in the XRD pattern (Fig. 4(a) and (b)). These split peaks correspond to a scheelite-to-fergusonite back transition, which was confirmed by the XRD refinement result collected at 0.1 GPa (Fig. 4(c)). It is very interesting to note that the pressure-induced zircon-to-scheelite transition is not reversible; the scheelite phase would always go back to fergusonite upon decompression. At this point, we conclude that both mf-$BiVO_4$ and tz-$BiVO_4$ transform to scheelite and β-fergusonite structures upon compression and go back to only mf-$BiVO_4$ when the pressure is released.

To understand the pressure-induced polymorphic transitions, the compressibility of each phase was examined using unit cell volume as a function of pressure. Fig. 5 depicts the experimental volume *vs.* pressure data for tz-$BiVO_4$. These data were fitted using the 3rd-order Birch–Murnaghan (B–M) equation of state (EOS) by fixing the first derivative of bulk modulus at $B_0' = 4$. The ambient pressure bulk modulus B_0 and volume V_0 obtained are also given in Table 1. From the fitting results, the EOS for different types of $BiVO_4$ have been determined. The bulk modulus B_0 = 105.2 GPa and the zero-pressure unit cell

Table 1 Crystal structures and unit cell parameters of $BiVO_4$ at different pressures obtained from XRD Rietveld refinement. The XRD data were collected during the course of compressing the tz-$BiVO_4$ sample from ambient pressure and decompressing the final product to ambient pressure

Space group	$I4_1/amd$	$I4_1/a$	$C2/c$	$I2/a$
P	1 atm	6.4 GPa	41.6 GPa	r 1 atm
a (Å)	7.29	5.086	4.858	5.169
b (Å)	7.29	5.086	11.189	5.086
c (Å)	6.45	11.477	4.252	11.497
β (°)	90	90	89.264	90
Bi	(0, 0.75, 0.25)	(0, 0.25, 0.625)	(0.50, 0.402, 0.25)	(0, 0.25, 0.635)
V	(0, 0.25, 0.375)	(0, 0.25, 0.125)	(0, 0.683, 0.25)	(0, 0.25, 0.155)
O	(0, 0.072, 0.214)	(0.179, 0.062, 0.261)	(0.675, 0.879, 0.079)	(0.305, 0.637, 0.125)
O			(0.372, 0.158, 0.985)	(0.324, 0.344, 0.440)
V_0 (Å^3)	342.6	306.1	275.9	302.3
B_0 (GPa)	101.1	116.3	125.2	111.5[43]
ρ (g cm^{-3})	6.28	7.03	7.80	7.12
R_p (%)	6.14	7.58	7.87	6.92
R_{wp} (%)	9.42	9.43	10.47	11.72

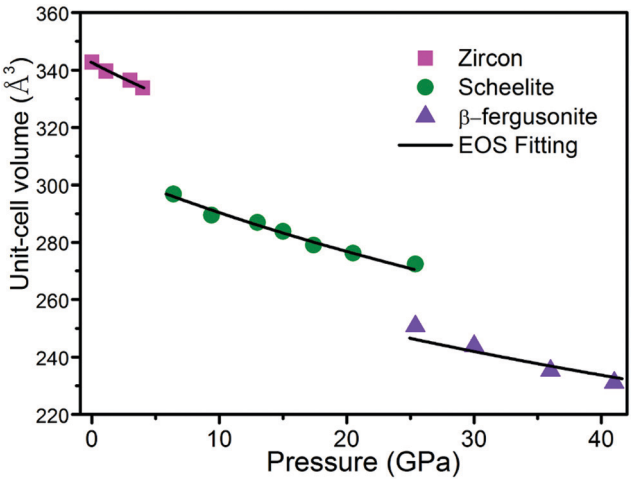

Fig. 5 The pressure dependence of the relative unit cell volume was fitted to the third-order Birch–Murnaghan equation of state.

volume V_0 = 342.6 Å^3 for tz-$BiVO_4$ were obtained. The transition from zircon to scheelite involves a volume collapse of approximately 11%, and a larger bulk modulus B_0 = 116.3 GPa for ts-$BiVO_4$. The volume change at the second transition is 8%. Therefore, a high-density β-fergusonite phase is obtained after two HP transitions. The bulk modulus of the β-fergusonite phase is 125.2 GPa, 23.8% larger than that of the initial zircon phase. These values agree well with the theoretical reported values of 103–132 GPa for different polymorphs of $BiVO_4$.[43]

3.3 Calculations of high-pressure phases of $BiVO_4$

To explore other possible high-pressure structures of $BiVO_4$, the enthalpy–pressure relations of the $BiVO_4$ structures were calculated and are shown in Fig. 6. Along with scheelite, zircon, fergusonite, β-fergusonite, and *Cmca* structures, we also considered other structures in related compound groups,

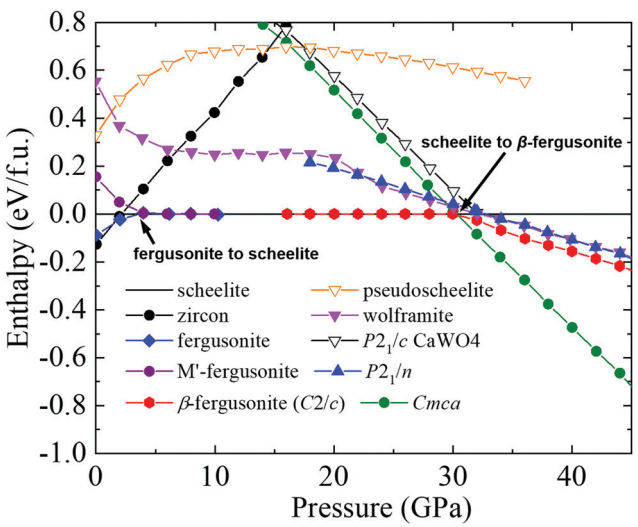

Fig. 6 Enthalpy difference as a function of pressure showing the phase transitions. The scheelite-phase was taken as a zero-energy reference (horizontal black line).

including pseudo-scheelite (*P*4/*nnc*), wolframite ($P2_1/c$), $P2_1/n$, M′-fergusonite (*P*2/*a*), and $CaWO_4$-type.[44–46] From an energetic consideration, tz-$BiVO_4$ and mf-$BiVO_4$ will transform to ts-$BiVO_4$ at around 2 GPa and 5 GPa, respectively. Such transition pressures are very close to the experimental values, *i.e.*, 1.3 GPa and 3.2 GPa. Above 15 GPa, scheelite and β-fergusonite structures have similar enthalpies (indistinguishable in this energy scale), which allows for their coexistence. Below 15 GPa, the β-fergusonite structure would collapse spontaneously to the scheelite structure in the optimization calculation, and therefore its enthalpy in the low-pressure range cannot be obtained. The enthalpy of β-fergusonite becomes lower than scheelite near 30 GPa, indicating a final phase transition in this neighborhood. The predicted theoretical phase transition sequence agrees very well with our experimental observation. Interestingly, β-fergusonite is not the lowest-enthalpy structure in the pressure range of interest. However, the phonon dispersion relations of β-fergusonite show no sign of an imaginary frequency (Fig. S4, ESI†), suggesting that this structure is mechanically and thermodynamically stable. The β-fergusonite structure should therefore be considered as a metastable phase stabilized by kinetics. At 30 GPa, metadynamics simulation reveals another phase transition from β-fergusonite to a structure with the *Cmca* space group, which does not belong to any known structures of orthovanadates. The calculated phonon dispersion relation for the *Cmca* structure shows no imaginary frequency throughout the BZ (Fig. S5, ESI†), suggesting that this structure is thermodynamically stable. The no-show of this structure in experiment indicates that it is dynamically blocked with a large activation barrier that requires significant over-compressing. Since the scheelite-to-β-fergusonite transition is just completed at 41.6 GPa, it is reasonable to speculate that the *Cmca* structure will form at higher pressure. The different value from theoretical calculation may be attributed to the non-hydrostatic condition in practice. We therefore propose the β-fergusonite to *Cmca* transition as a prediction, encouraging future experimental confirmation. In addition, the $P2_1/n$ structure is a distorted version of *C*2/*c* with a higher enthalpy. From both experimental fitting and theoretical calculation, the β-fergusonite *C*2/*c* structure may be a better candidate because it is dynamically related to the low pressure structure, *i.e.*, it is linked by molecular dynamics through an explainable path.

3.4 Discussion

Fig. 7 shows the observed structural evolution of $BiVO_4$ under pressure. Although all four structures are composed of BiO_8 dodecahedra and VO_4 tetrahedra, their arrangements are quite different. In zircon and scheelite structures, BiO_8 dodecahedra have two different Bi–O distances, while the four V–O bonds in VO_4 tetrahedron are identical. In the zircon structure, the *c*-axis is formed by alternating VO_4 tetrahedra and BiO_8 dodecahedra, while the *a*-axis is formed by only edge-sharing BiO_8 dodecahedra, resulting in the *c* axis being less compressible than the *a* axis.[14,16,47] In contrast, in the scheelite structure, the VO_4 tetrahedra are aligned along the *a*-axis, whereas BiO_8 dodecahedra are intercalated with VO_4 tetrahedra along the *c* axis.[47]

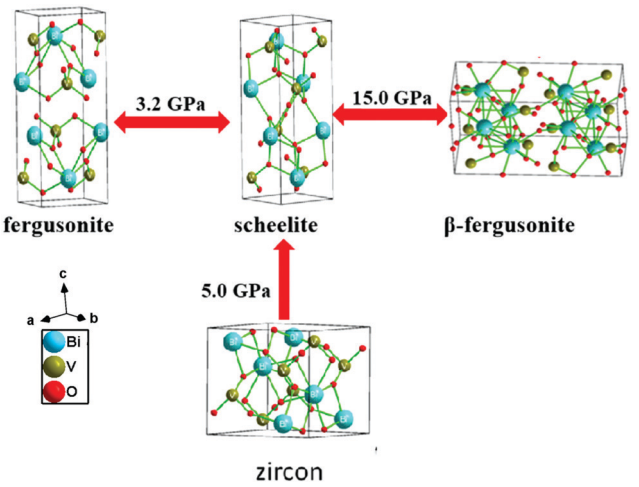

Fig. 7 Schematic model for the phase transition of $BiVO_4$ upon compression.

Therefore, in the scheelite structure, the *a*-axis is less compressible. During the zircon-to-scheelite transformation, the [110] direction of zircon is converted to the [001] direction of scheelite by a simple shearing mechanism, resulting in a distortion in the VO_4 tetrahedra because of a pressure-induced contraction,[48] which can be confirmed from the volume collapse of approximately 11% shown in Fig. 5. Consequently, pressure induces a rearrangement of the VO_4 and BiO_8 units during the zircon-to-scheelite phase transition.

The change of the β angle during the scheelite-to-β-fergusonite transition indicates that the monoclinic distortion of fergusonite gradually increases under compression. In fergusonite $BiVO_4$, the V cation is tetrahedrally coordinated to oxygen anions with two different bond lengths, and the Bi cation is coordinated to eight oxygen anions with four different bond lengths, resulting in a lower symmetry. Therefore, during the fergusonite–scheelite transition, the structure symmetry increases, resulting in the merging of several split Raman peaks and XRD peaks, as shown in Fig. 1 and 4. During this phase transition, the tetrahedral coordination of V is retained, which is accompanied by a slight distortion of the VO_4 tetrahedron. It has been pointed out that this phase transition may be driven by the lone-pair Bi^{3+} cation due to the recovery of the distorted dodecahedron and to a lesser extent the VO_4 tetrahedra.[4] Upon further increasing pressure, ts-$BiVO_4$ will convert into another fergusonite structure, β-fergusonite, which is known in mineralogy of $YNbO_4$. Similar to fergusonite, β-fergusonite has also a slight distortion of the scheelite structure with two distinct V–O bonds and four distinct Bi–O bonds. The scheelite to β-fergusonite transition is a first-order reconstructive transformation, resulting in a large volume collapse of about 8%. Consequently, splitting of several initial diffraction peaks in ts-$BiVO_4$ is observed above 15 GPa during this transition.

It has been proposed that the zircon–scheelite–fergusonite (Z–S–F) transition is a common behavior for most orthovanadate materials under high pressure.[16,46] However, $BiVO_4$ exhibits different transition sequences, either fergusonite to scheelite to β-fergusonite, or zircon to scheelite to β-fergusonite. Both starting structures would reach the same β-fergusonite structure under sufficient compression. As discussed above, pressure causes a rearrangement of the VO_4 and BiO_8 units during zircon-to-scheelite transition, resulting in a larger activation barrier. In contrast, the fergusonite-to-scheelite transition is associated with a smaller barrier since only a slight structural distortion is involved. This thermodynamic preference determines that the scheelite structure would transform back to fergusonite rather than the zircon structure during the pressure release. Moreover, from the theoretical prediction (Fig. 6), a new *Cmca* phase is found to be energetically more favorable for $BiVO_4$ even at a higher pressure. Thus, it is of great interest to examine the possible new polymorphs of $BiVO_4$ in an extended pressure region in the future.

4. Conclusions

Fergusonite- and zircon-type $BiVO_4$ materials are successfully synthetized using the hydrothermal method. The high-pressure structural stabilities of both polymorphs have been investigated at room temperature by using *in situ* high-pressure XRD, Raman spectroscopy, and *ab initio* calculations. The Raman and XRD results revealed two consecutive reversible transitions for fergusonite $BiVO_4$, namely fergusonite to scheelite and scheelite to a new HP phase at 3.2 GPa and 15.0 GPa, respectively. For the zircon-type $BiVO_4$, an irreversible zircon-to-scheelite transition starts at 1.3 GPa and completes at 5.0 GPa. The second transition to the same new HP phase also starts above 15.0 GPa and completes around 41.6 GPa. The new HP phase was successfully identified as β-fergusonite by using metadynamics simulations and refinement of the XRD data. Theoretical enthalpy calculations confirmed the experimental transition sequence and predicted a new high-pressure phase at higher pressures. The high-pressure structure of zircon-type $BiVO_4$ transformed back to the fergusonite structure upon decompression, indicating that the fergusonite structure is the most stable phase among all known polymorphs of $BiVO_4$. The pressure dependence of the unit-cell parameters has been extracted, and the equations of state of different phases were also determined. The high-pressure behavior of $BiVO_4$ is different from other orthovanadates, which contributes to a more in-depth understanding of the pressure behavior of AVO_4 compounds.

Conflicts of interest

There are no conflicts to declare.

Acknowledgements

We gratefully acknowledge the financial support of the National Natural Science Fund of China (No. 11404292), Key Research Project of the Department of Science and Technology in Henan Province (No. 192102210003) and the Program for Innovative Research Team (in Science and Technology) in the

University of Henan Province (No. 20IRTSTHN017). We acknowledge the Natural Science and Engineering Research Council of Canada (NSERC) for Discovery Grants (Y. S. and Y. Y.), and a Leading Opportunity Fund from the Canadian Foundation for Innovation (Y. S.). Computing resources were provided by the University of Saskatchewan and Compute Canada. The synchrotron micro-diffraction was performed at HPCAT (Sector 16), Advanced Photon Source (APS), Argonne National Laboratory under the support of Capital/DOE Alliance Center (CDAC). HPCAT operations are supported by the DOE-NNSA's Office of Experimental Sciences.

References

1 C. M. Ding, J. Y. Shi, D. G. Wang, Z. J. Wang, N. Wang, G. J. Liu, F. Q. Xiong and C. Li, *Phys. Chem. Chem. Phys.*, 2013, **15**, 4589–4595.
2 L. Zhou, W. Z. Wang, L. Zhang, H. L. Xu and W. Zhu, *J. Phys. Chem. C*, 2007, **111**, 13659–13664.
3 S. J. Hong, S. Lee, J. S. Jang and J. S. Lee, *Energy Environ. Sci.*, 2011, **4**, 1781–1787.
4 D. Zhou, L. X. Pang, D. W. Wang and I. M. Reaney, *J. Mater. Chem. C*, 2018, **6**, 9290–9313.
5 G. Q. Tan, L. L. Zhang, H. J. Ren, S. S. Wei, J. Huang and A. Xia, *ACS Appl. Mater. Interfaces*, 2013, **5**, 5186–5193.
6 P. Li, X. Y. Chen, H. C. He, X. Zhou, Y. Zhou and Z. G. Zou, *Adv. Mater.*, 2018, **30**, 1703119.
7 Y. Y. Luo, G. Q. Tan, G. H. Dong, H. J. Ren and A. Xia, *Appl. Surf. Sci.*, 2016, **364**, 156–165.
8 L. X. Pang, D. Zhou, Z. M. Qi, W. G. Liu, Z. X. Yue and I. M. Reaney, *J. Mater. Chem. C*, 2017, **5**, 2695–2701.
9 D. Zhou, W. B. Li, H. H. Xi, L. X. Pang and G. S. Pang, *J. Mater. Chem. C*, 2015, **3**, 2582–2588.
10 X. R. Cheng, Y. F. Ren, J. M. Shang and Y. Song, *J. Phys. Chem. C*, 2017, **121**, 723–730.
11 J. Pellicer-Porres, D. Vazquez-Socorro, S. Lopez-Moreno, A. Munoz, P. Rodriguez-Hernandez, D. Martinez-Garcia, S. N. Achary, A. J. E. Rettie and C. B. Mullins, *Phys. Rev. B: Condens. Matter Mater. Phys.*, 2018, **98**, 214109.
12 V. Panchal, F. J. Manjon, D. Errandonea, P. Rodriguez-Hernandez, J. Lopez-Solano, A. Munoz, S. N. Achary and A. K. Tyagi, *Phys. Rev. B: Condens. Matter Mater. Phys.*, 2011, **83**, 064111.
13 C. C. Zhang, Z. M. Zhang, R. C. Dai, Z. P. Wang, J. W. Zhang and Z. J. Ding, *J. Phys. Chem. C*, 2010, **114**, 18279–18282.
14 D. Errandonea, R. Lacomba-Perales, J. Ruiz-Fuertes, A. Segura, S. N. Achary and A. K. Tyagi, *Phys. Rev. B: Condens. Matter Mater. Phys.*, 2009, **79**, 184104.
15 A. B. Garg, D. Errandonea, P. Rodriguez-Hernandez, S. Lopez-Moreno, A. Munoz and C. Popescu, *J. Phys.: Condens. Matter*, 2014, **26**, 265402.
16 D. Errandonea, F. J. Manjon, A. Munoz, P. Rodriguez-Hernandez, V. Panchal, S. N. Achary and A. K. Tyagi, *J. Alloys Compd.*, 2013, **577**, 327–335.
17 F. J. Manjon, P. Rodriguez-Hernandez, A. Munoz, A. H. Romero, D. Errandonea and K. Syassen, *Phys. Rev. B: Condens. Matter Mater. Phys.*, 2010, **81**, 075202.
18 A. B. Garg, K. V. Shanavas, B. N. Wani and S. M. Sharma, *J. Solid State Chem.*, 2013, **203**, 273–280.
19 R. Mittal, A. B. Garg, V. Vijayakumar, S. N. Achary, A. K. Tyagi, B. K. Godwal, E. Busetto, A. Lausi and S. L. Chaplot, *J. Phys.: Condens. Matter*, 2008, **20**, 075223.
20 R. M. Hazen and J. W. E. Mariathasan, *Science*, 1982, **216**, 991.
21 A. Pinczuk, B. Welber and F. H. Dacol, *Bull. Am. Phys. Soc.*, 1978, **23**, 196.
22 J. W. E. Mariathasan, R. M. Hazen and L. W. Finger, *Phase Transitions*, 1986, **6**(3), 165.
23 D. Errandonea, A. B. Garg, J. Pellicer-Porres, D. Martinez-Garcia and C. Popescu, *J. Phys.: Condens. Matter*, 2019, **31**, 485401.
24 L. Wang, Y. Pan, Y. Ding, W. Yang, W. L. Mao, S. V. Sinogeikin, Y. Meng, G. Shen and H.-k. Mao, *Appl. Phys. Lett.*, 2009, **94**, 061921.
25 Z.-W. Chen, J.-S. Lee, T. Huang and C.-M. Lin, *Solid State Commun.*, 2012, **152**, 1613–1617.
26 S. F. F. Grinblat, L. G. Pampillo, F. D. Saccone, D. Errandonea, D. Santamaria-Perez, A. Segura, R. Vilaplana and C. Popescu, *Solid State Sci.*, 2017, **64**, 91–98.
27 R. Z. P. Wang, L. Wu and M. Zhang, *RSC Adv.*, 2017, **7**, 35105.
28 Y. Y. Luo, G. Q. Tan, G. H. Dong, L. L. Zhang, J. Huang, W. Yang, C. C. Zhao and H. J. Ren, *Appl. Surf. Sci.*, 2015, **324**, 505–511.
29 S. N. Gu, W. J. Li, F. Z. Wang, H. D. Li and H. L. Zhou, *Catal. Sci. Technol.*, 2016, **6**, 1870–1881.
30 S. Usai, S. Obregon, A. I. Becerro and G. Colon, *J. Phys. Chem. C*, 2013, **117**, 24479–24484.
31 R. Z. Chen, P. Wu, X. M. Ma and D. M. Jiang, *RSC Adv.*, 2016, **6**, 34666–34673.
32 Q. G. Wei, N. Dubrovinskaia and L. Dubrovinsky, *J. Appl. Phys.*, 2011, **110**, 043513.
33 A. V. Arzhannikov, V. V. Boldyrev, A. V. Burdakov, I. A. Ivanov, V. S. Koidan, V. V. Postupaev, A. F. Rovenskikh, S. V. Polosatkin, S. L. Sinitskii and A. A. Shoshin, *Instrum. Exp. Tech.*, 2006, **49**, 293–296.
34 R. Martonak, D. Donadio, A. R. Oganov and M. Parrinello, *Nat. Mater.*, 2006, **5**, 623–626.
35 R. Martonak, A. Laio and M. Parrinello, *Phys. Rev. Lett.*, 2003, **90**, 075503.
36 G. Kresse and J. Hafner, *Phys. Rev. B: Condens. Matter Mater. Phys.*, 1993, **47**, 558–561.
37 G. Kresse and D. Joubert, *Phys. Rev. B: Condens. Matter Mater. Phys.*, 1999, **59**, 1758–1775.
38 J. P. Perdew, K. Burke and M. Ernzerhof, *Phys. Rev. B: Condens. Matter Mater. Phys.*, 1996, **77**, 3865.
39 Y. Yao and D. D. Klug, *Phys. Rev. B: Condens. Matter Mater. Phys.*, 2012, **85**, 214122.
40 S. Baroni, S. de Gironcoli and A. Dal Corso, *Rev. Mod. Phys.*, 2001, **73**, 515–562.

41 A. Togo and I. Tanaka, *Scr. Mater.*, 2015, **108**, 1–5.
42 D. Zhou, L. X. Pang, J. Guo, Z. M. Qi, T. Shao, X. Yao and C. A. Randall, *J. Mater. Chem.*, 2012, **22**, 21412–21419.
43 A. K. M. Farid Ul Islam, M. A. Helal, M. N. H. Liton, M. Kamruzzaman and H. M. Tariqul Islam, *Chin. Phys. B*, 2017, **26**, 036301.
44 D. Errandonea, F. J. Manjón, N. Garro, P. Rodríguez-Hernández, S. Radescu, A. Mujica, A. Muñoz and C. Y. Tu, *Phys. Rev. B: Condens. Matter Mater. Phys.*, 2008, **78**, 054116.
45 P. Botella, R. Lacomba-Perales, D. Errandonea, A. Polian, P. Rodriguez-Hernandez and A. Munoz, *Inorg. Chem.*, 2014, **53**, 9729–9738.
46 D. Errandonea and A. B. Garg, *Prog. Mater. Sci.*, 2018, **97**, 123–169.
47 A. B. Garg and D. Errandonea, *J. Solid State Chem.*, 2015, **226**, 147–153.
48 B. B. Yue, F. Hong, S. Merkel, D. Y. Tan, J. Y. Yan, B. Chen and H. K. Mao, *Phys. Rev. Lett.*, 2016, **117**, 135701.